

Lawrence Berkeley National Laboratory

Recent Work

Title

Extraordinary Redox Activities in Ladder-Type Conjugated Molecules Enabled by B \leftarrow N Coordination-Promoted Delocalization and Hyperconjugation.

Permalink

<https://escholarship.org/uc/item/8t9115v7>

Journal

Journal of the American Chemical Society, 140(51)

ISSN

0002-7863

Authors

Zhu, Congzhi
Ji, Xiaozhou
You, Di
[et al.](#)

Publication Date

2018-12-01

DOI

10.1021/jacs.8b11337

Peer reviewed

Extraordinary Redox Activities in Ladder-Type Conjugated Molecules Produced by B \leftarrow N Coordination-Promoted Delocalization and Hyperconjugation

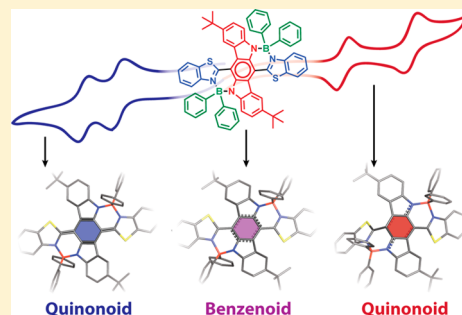
Congzhi Zhu,[†] Xiaozhou Ji,[†] Di You,[†] Teresa L. Chen,[§] Anthony U. Mu,[†] Kayla P. Barker,[†] Liana M. Klivansky,[§] Yi Liu,[§] and Lei Fang^{*,†,‡,§}

[†]Department of Chemistry and [‡]Department of Materials Science and Engineering, Texas A&M University, 3255 TAMU, College Station, Texas 77843, United States

[§]The Molecular Foundry, Lawrence Berkeley National Laboratory, One Cyclotron Road, Berkeley, California 94720, United States

Supporting Information

ABSTRACT: The introduction of B \leftarrow N coordination—isolectronic to C—C single bond—into π -systems represents a promising strategy to impart exotic redox and electrochromic properties into conjugated organic molecules and macromolecules. To achieve both reductive and oxidative activities using this strategy, a cruciform ladder-type molecular constitution was designed to accommodate oxidation-active, reduction-active, and B \leftarrow N coordination units into a compact structure. Two such compounds (BN-F and BN-Ph) were synthesized via highly efficient N-directed borylation. These molecules demonstrated well-separated, two-reductive and two-oxidative electron-transfer processes, corresponding to five distinct yet stable oxidation states, including a rarely observed boron-containing radical cation. Spectroelectrochemical measurements revealed unique optical characteristics for each of these reduced/oxidized species, demonstrating multicolor electrochromism with excellent recyclability. Distinct color changes were observed between each redox state with clear isosbestic points on the absorption spectra. The underlying redox mechanism was elucidated by a combination of computational and experimental investigations. Single-crystal X-ray diffraction analysis on the neutral state, the oxidized radical cation, and the reduced dianion of BN-Ph revealed structural transformations into two distinct quinonoid constitutions during the oxidation and reduction processes, respectively. B \leftarrow N coordination played an important role in rendering the robust and reversible multistage redox properties, by extending the charge and spin delocalization, by modulating the π -electron density, and by a newly established hyperconjugation mechanism.



INTRODUCTION

Ladder-type conjugated molecules, constituted with an uninterrupted sequence of fused adjacent rings that share two or more atoms with one another, have shown great promise for applications on multiple fronts that demand superior optical, electronic, or mechanical properties.^{1–10} Stemming from the strong intramolecular electronic couplings throughout fused conjugated backbones, ladder-type conjugated compounds also demonstrate intriguing electrochemical behaviors, such as the capability of undergoing multiple electron transfers.^{7,11} The extended conjugation and rigid backbones can greatly stabilize the highly reactive radical and ionic intermediates that are generated during the redox processes. For instance, ladder-type oligothiophene exhibited stepwise oxidations.^{7,12} A recently reported series of ladder-type conjugated polycyclic hydrocarbons, featuring extensive graphitic constitutions, demonstrated four distinct reversible redox processes.¹³ In this context, ladder-type molecular design represents an important strategy to achieve exotic molecular materials desirable for sophisticated electrochemical applications.^{11,14,15}

To date, redox-active ladder-type compounds are mostly fused with entirely covalent bonds.^{1,3,4} Alternatively, intramolecular noncovalent B \leftarrow N coordination^{16–19} has been exploited to serve as a bridge to construct ladder-type conjugated molecules while imparting modification to the aromatic character.^{20,21} Compared to the isoelectronic and isosteric C—C single bond, intramolecular B \leftarrow N coordination in a conjugated molecule not only extends the π -delocalization but also dramatically changes the electronic structures, electronic and optical properties,^{17–19,22–32} and reactivities,^{33,34} because of the intrinsically different valence electron configurations and electronegativities of boron and nitrogen compared to carbon. For instance, the incorporation of B \leftarrow N coordination into conjugated molecules deepens the lowest unoccupied molecular orbital (LUMO) energy levels, which facilitate reductive electron-transfer processes.^{17,19,25–27,35} Additionally, boron atoms can couple with a neighboring unpaired spin, providing additional stabilization effects for

Received: October 21, 2018

Published: December 3, 2018

radical intermediates during redox processes.^{35–38} Therefore, the employment of B ← N coordination represents a powerful strategy to develop novel conjugated molecules and macro-molecules with new redox properties that were not accessible before.

Despite the great potential of this noncovalent approach, however, it is still challenging to achieve robust redox activities in B ← N bridged ladder-type molecules, especially oxidation processes, because of the electron-deficient nature of boron moieties and the resulting low stability of the corresponding oxidized states. Meanwhile, the underlying mechanism of the redox processes of B ← N bridged ladder-type molecules remains unclear, especially on the impacts of tetracoordinated boron centers on the electronic structures and optical characteristics of these molecules. Herein, we report a molecular design strategy that allowed for the access to five redox states, both reduced and oxidized, of B ← N bridged ladder-type molecules, as well as the corresponding mechanistic investigations.

RESULTS AND DISCUSSION

To pursue both robust reductive and oxidative electron-transfer processes in B ← N bridged ladder-type molecules, we envisioned that the molecular design should first integrate multiple redox-active components in an orthogonal and compact manner, so that multiple electron-transfer processes can be enabled in a small molecule without interfering with each other. Second, B ← N coordination needs to be installed to rigidify the π -system to facilitate the desired delocalization of charges and spins, therefore stabilizing the reduced or oxidized species. On the basis of these principles, we designed a ladder-type molecule composed of an oxidation-active indolo[3,2-*b*]carbazole (ICBZ) unit and two reduction-active benzo[*d*]thiazole (BTH) units (Figure 1a). The ICBZ unit is

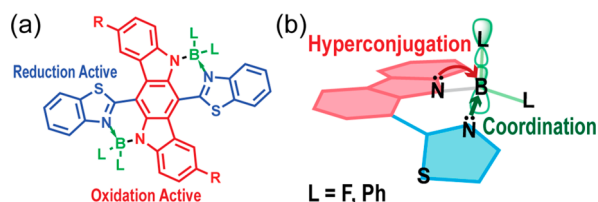
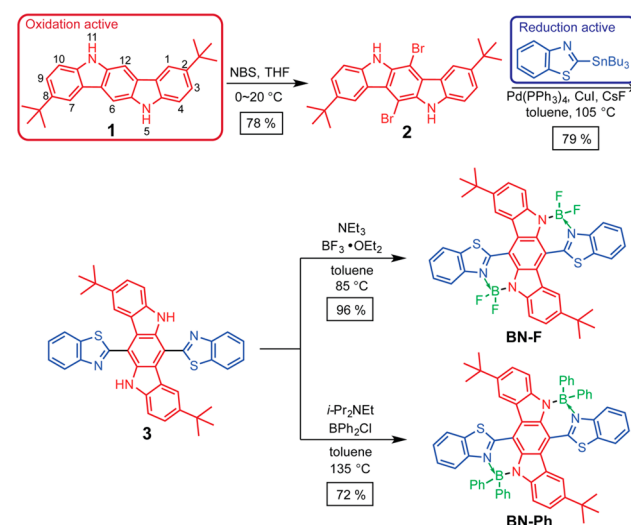


Figure 1. (a) Designed ladder-type molecule featuring cruciform arrangement of redox-active units (reduction-active in blue and oxidation-active in red) and B ← N coordination that can rigidify and coplanarize the entire molecule; (b) representative orbital interactions of the boron center in the designed conjugated backbone.

The B ← N coordination in this molecular design was formed in a geometrically favored six-membered heterocycle architecture, which fused the ICBZ and BTH units into a ladder-type structure. The N–B ← N constitution was expected to be stable not only in ambient condition but also during redox processes, similar to the known stability of BODIPY dyes.^{45,46} The strong B ← N coordination significantly withdrew the electron density from BTH units, resulting in an enhanced electron affinity.^{17,19,25} Consequently, the reduction of such a molecule could fall into an accessible potential range. Moreover, this boron-containing six-membered heterocycle architecture reassembles the structure of cyclohexa-1,3-diene, in which a series of hyperconjugative interactions were previously observed to significantly impact the molecular conformation, properties, and stability.^{47,48} In this design, the sp^3 hybridized boron atom carried two ligands that were expected to undergo hyperconjugative interactions similar to those existing in cyclohexa-1,3-diene (Figure 1b). We hypothesized that these hyperconjugative interactions could further stabilize the radical intermediates upon reduction/oxidation, by assisting the charge and spin delocalization. Consequently, the low-energy singly occupied molecular orbital (SOMO) to LUMO transition of these stabilized organic radicals could be utilized to achieve electrochromism in the near-infrared (NIR) region,⁴⁹ which is highly desired for various applications including data storage, smart windows, and sensing.^{11,50–52}

On the basis of this design principle, two molecular candidates, BN-F and BN-Ph, with fluoride and phenyl groups attached to the boron center as ligands, respectively, were synthesized. The syntheses were accomplished (Scheme 1) in

Scheme 1. Synthesis of BN-F and BN-Ph



three steps starting from 2,8-di-*tert*-butyl-5,11-dihydroindolo[3,2-*b*]carbazole (compound 1). First of all, treatment of 1 with 2.0 equiv of *N*-bromosuccinimide (NBS) selectively brominated the 6- and 12-positions to give a dibromo derivative, 2. Compound 2 was subsequently subjected to Stille coupling reaction with 2-(tributylstannyl)benzo[*d*]thiazole. CuI and CsF were used to facilitate the transmetalation step⁵³ during the Stille reaction to give intermediate 3. In this step, temperature control was crucial to achieve a high yield. Significant side reactions were found above 130 °C,

157 which was likely a result of undesired copper-catalyzed
 158 reactions, such as Ullmann coupling.⁵⁴ Finally, borylation of
 159 **3** with BF_3 and BPh_2Cl in the presence of non-nucleophilic
 160 bases afforded the desired products in excellent isolated yields
 161 (96% and 72%, respectively). Notably, the isolation yield of
 162 **BN-Ph** was significantly improved compared to a previously
 163 reported reaction using BPh_3 to introduce $\text{B} \leftarrow \text{N}$ coordinate
 164 bonds into a similar ICBZ backbone,⁴³ likely due to the higher
 165 electrophilicity and smaller steric hindrance of BPh_2Cl . **BN-F**
 166 and **BN-Ph** showed good stabilities in ambient conditions. For
 167 example, **BN-Ph** was purified by normal-phase silica gel
 168 chromatography. Both final products were fully characterized
 169 by NMR spectroscopy and mass spectrometry. In addition,
 170 **BN-Ph** was characterized unambiguously by single-crystal X-
 171 ray diffraction analysis. Single crystals of **BN-Ph** suitable for X-
 172 ray diffraction analysis were obtained by vapor diffusion of
 173 pentane into a chloroform solution. Tetrahedral geometry of
 174 the boron centers was revealed, with a short $\text{B} \leftarrow \text{N}$ coordinate
 175 bond length of 1.643 Å. The anticipated rigid conformation of
 176 **BN-Ph** bridged by the $\text{B} \leftarrow \text{N}$ coordination was validated in
 177 the solid-state crystal structure. The dihedral angles between
 178 ICBZ units and BTH units were measured to be 20.0° in **BN-Ph**,
 179 significantly smaller than that observed in the density
 180 functional theory (DFT) computed, energy-minimized geom-
 181 etry of the precursor **3** (Figure S12).

182 DFT calculations on the π -conjugated backbone revealed
 183 extended π -delocalization on **BN-F** and **BN-Ph**. The visualized
 184 highest occupied molecular orbitals (HOMOs) of both
 185 molecules were delocalized over the entire conjugated
 186 backbones with non-negligible contributions from the boron
 187 centers and the ligands (Figure S11). The majority of LUMOs
 188 were on the electron-deficient BTH units and the boron
 189 centers. Time-dependent DFT calculations afforded multiple
 190 optical transitions with significant intensities, including the
 191 lowest band gap $\text{HOMO} \rightarrow \text{LUMO}$ transitions, and the
 192 higher-energy $\text{HOMO}-1 \rightarrow \text{LUMO}$ transitions. These
 193 transitions matched well with experimental spectra. Both
 194 **BN-F** and **BN-Ph** possessed low band gap NIR absorptions
 195 and fluorescent emissions. For example, the UV-vis-NIR
 196 spectrum of a dilute solution of **BN-F** in CH_2Cl_2 showed the
 197 low-energy $\text{HOMO} \rightarrow \text{LUMO}$ absorption peak at 695 nm ($\epsilon =$
 198 $1.17 \times 10^4 \text{ M}^{-1}\text{cm}^{-1}$) (Figure 2a). For **BN-Ph** with phenyl
 199 ligands on the boron center, such $\text{HOMO} \rightarrow \text{LUMO}$ band
 200 red-shifted into the NIR region ($\lambda_{\text{max}} = 768 \text{ nm}$, $\epsilon = 1.80 \times 10^4$
 201 $\text{M}^{-1}\text{cm}^{-1}$) (Figure 2b). The presence of vibrational
 202 progression in both spectra indicated the rigid nature of **BN-Ph**
 203 **F** and **BN-Ph**.^{1,2} Fluorescence emission of **BN-F** and **BN-Ph**
 204 appeared in the NIR region with λ_{max} at 720 and 812 nm in
 205 CH_2Cl_2 , respectively (Figure 2a and b). Small Stokes shifts
 206 (576 cm^{-1} for **BN-F** and 705 cm^{-1} for **BN-Ph**) also implied
 207 their backbone rigidity, due to the lack of energy loss
 208 associated with conformational changes during the excita-
 209 tion-emission processes. The fluorescence quantum yields of
 210 **BN-F** and **BN-Ph** were measured using reference standards
 211 (zinc phthalocyanine for **BN-F** and indocyanine green for **BN-Ph**)
 212 to be 2.8% and 1.2% in CH_2Cl_2 , respectively.

213 On the basis of the molecular design, **BN-F** and **BN-Ph** were
 214 expected to undergo multistage electron-transfer processes.
 215 Indeed, cyclic voltammograms (CVs) unveiled four well-
 216 separated, reversible electron-transfer processes in both **BN-F**
 217 and **BN-Ph** (Figure 3), indicating five accessible redox states
 218 for both compounds. The excellent reversibility of these
 219 processes indicated the high stability of all the states including

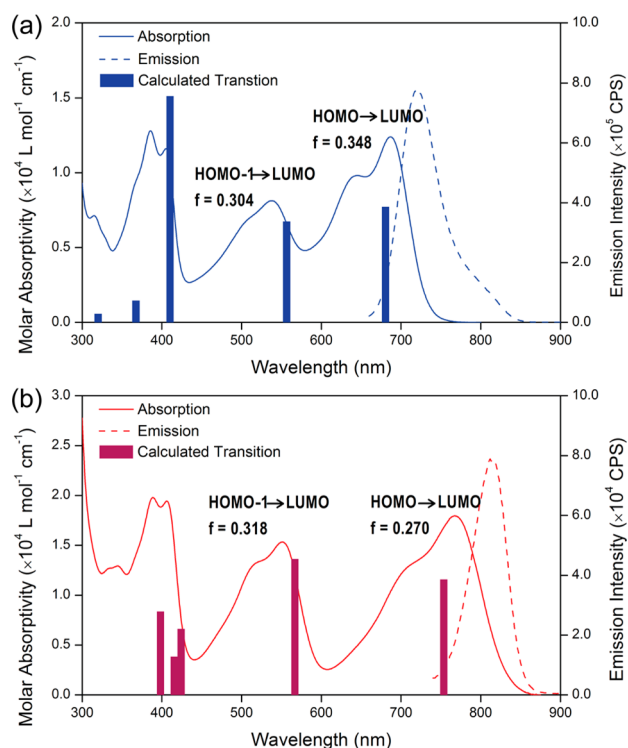


Figure 2. UV-vis-NIR absorption (solid lines) and emission (dashed lines) of (a) **BN-F** and (b) **BN-Ph** in CH_2Cl_2 with transition energies calculated by time-dependent DFT (TD-DFT) using B3LYP/6-311g(d,p) with CH_2Cl_2 CPCM solvation.

radical anions (-1), dianions (-2), radical cations ($+1$), and
 220 dications ($+2$). The measured electrochemical band gaps of
 221 **BN-F** and **BN-Ph** (1.81 and 1.62 eV, respectively) matched
 222 well with the optical band gap (1.78 and 1.60 eV, respectively).
 223 Among these two voltammograms, the redox processes of **BN-Ph**
 224 appeared cathodically shifted (Figure 3b) compared to that
 225 of **BN-F**, likely due to the more electron-rich nature of the
 226 phenyl ligand compared to fluoride. Such an effect was more
 227 significant on the oxidation processes, leading to a narrower
 228 band gap of **BN-Ph** than that of **BN-F**.

229 All the anodic and cathodic peaks of **BN-F** and **BN-Ph**
 230 during both oxidation and reduction sweeps were well-
 231 separated, suggesting the good stabilities of the radical anion
 232 and radical cation intermediates toward disproportionation.
 233 For example, the potential gaps between the two reduction
 234 waves for both **BN-F** and **BN-Ph** were $\sim 0.3 \text{ V}$ (Figure 3a and
 235 b). These values corresponded to large radical comproportion-
 236 ation constants of the reduced forms ($K_{\text{com-re}}$) of 5.41×10^4
 237 for **BN-F** and 1.74×10^5 for **BN-Ph** at 25°C (equilibrium 1 in
 238 Figure 3d), indicating a highly stable radical anion. On the
 239 oxidation side, the potential gaps between the two oxidative
 240 processes were even larger (0.45 V for **BN-F** and 0.51 V for
 241 **BN-Ph**), corresponding to remarkably high radical compro-
 242 portionation constants ($K_{\text{com-ox}}$) of 4.04×10^7 and 4.17×10^8
 243 at 25°C , respectively (equilibrium 2 in Figure 3d). Such high
 244 stabilities of the radicals were attributed to the strong spin-
 245 delocalization on the rigid backbones of **BN-F** and **BN-Ph** as
 246 designed. In contrast, precursor **3** without $\text{B} \leftarrow \text{N}$
 247 coordination, as a control, showed overlapping two-electron
 248 oxidation processes (Figure 3c) and irreversible reduction
 249 processes. Such a drastic difference on the redox behaviors
 250 between **BN-F/BN-Ph** and **3** demonstrated profound changes

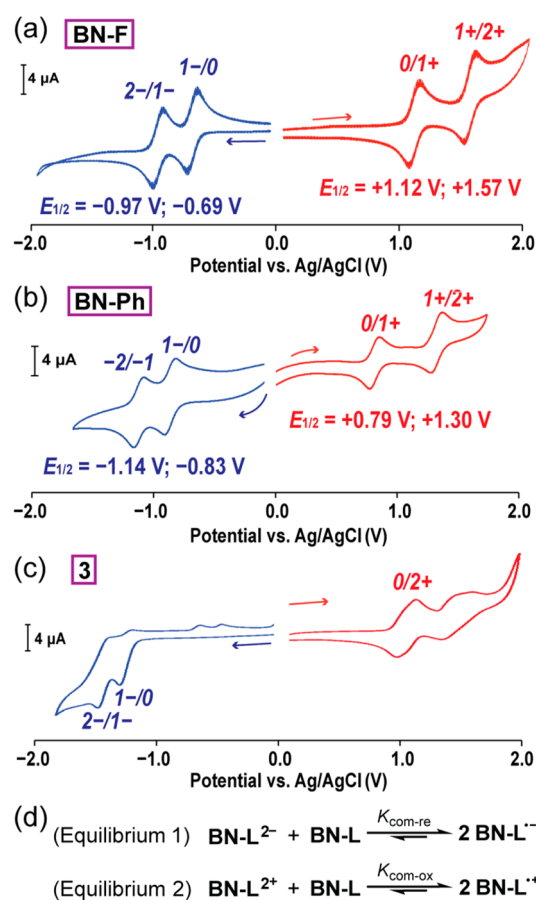


Figure 3. CV curves of (a) BN-F, (b) BN-Ph, and (c) 3 in CH_2Cl_2 [0.10 M tetrabutylammonium hexafluorophosphate (TBAPF₆) as the electrolyte; Ag/AgCl as the reference electrode; scan rate = 100 mV/s]. The half-wave potentials of each redox process were noted in (a) BN-F and (b) BN-Ph. (d) Comproportionation equilibria of radical cations and radical anions.

change from 1.05 to 1.25 V, indicating the good stability of $\text{BN-Ph}^{\bullet+}$ over a wide range of potentials. When $\text{BN-Ph}^{\bullet+}$ was oxidized into the dication form BN-Ph^{2+} by increasing the potential from 1.30 to 1.50 V, the characteristic radical cation absorption peak at 1180 nm gradually diminished, while multiple absorption bands covering a broad visible light region emerged (Figure 4c). To test the reversibility of these oxidation processes, iterative potential sweepings were conducted between +0.20, +1.10, and +1.50 V for >15 cycles (Figure 4h). Excellent reversibility was demonstrated without notable degradation of the absorption intensity (monitored at 470 nm).

Similarly, the radical anion and dianion of BN-Ph were investigated by spectroelectrochemistry study. Upon the application of a negative potential of -0.75 V, BN-Ph started to be reduced as the absorption intensity at 768 nm decreased (Figure 4e) while a highly intensive peak at 677 nm and a weak absorption peak at ~940 nm emerged, corresponding to the optical transitions, HOMO-1- α \rightarrow LUMO- α and HOMO- β \rightarrow LUMO- β of radical anion $\text{BN-Ph}^{\bullet-}$ (Figure 4g). The Gaussian shape of this low energy peak indicated that $\text{BN-Ph}^{\bullet-}$ was a class II mixed valence system, in which the two reduced BTH moieties were coupled in a weaker manner.^{55,56} Further decrease of the potential from -1.05 to -1.35 V resulted in the second step of reduction into the dianion, BN-Ph^{2-} , accompanied by the diminishing of all the peaks in the long-wavelength region and the emerging of a higher-energy peak centered at 544 nm as the new HOMO \rightarrow LUMO transition (Figure 4f). Again, excellent reversibility of the reduction processes was confirmed by monitoring the absorption intensity at 680 nm while sweeping the potential iteratively between -0.30, -1.05, and -1.40 V (Figure 4i) for >15 cycles. Spectroelectrochemical measurements were also conducted in a CH_2Cl_2 solution of BN-F, which showed a similar reversible multistage electrochromism over a wide range of electric potentials (Figure S9).

To shed light on the mechanism of these remarkable redox and electrochromic activities of BN-Ph and BN-F, DFT computations were performed starting with geometry optimization [B3LYP/6-311g(d,p)] for all five redox states of BN-Ph in the gas phase. At the neutral state of BN-Ph, the lengths of bonds *c*, *d*, and *e* in the central ring "A" (1.412–1.427 Å) were close to that in a benzene ring (Figure 5a). Upon oxidation into the radical cation $\text{BN-Ph}^{\bullet+}$, DFT calculation showed that the bond length alternation (BLA) between these three bonds increased, indicating a decrease of aromaticity. The BLA increased further in the diradical form BN-Ph^{2+} (Figure 5b), so that bonds *c* and *e* were elongated to 1.451 and 1.438 Å, respectively, while bond *d* was shortened to 1.388 Å, close to the bond length of a typical C=C double bond. Additionally, the C=N double bonds *b* and *f* were shortened from 1.366 Å in BN-Ph to 1.330 Å in BN-Ph^{2+} . This computational study revealed a tendency toward quinonoid character of the ICBZ unit after oxidation (Figure 5e). In contrast, optimized geometries of the reduced forms exhibited that a different quinonoid structure was formed in between the two BTH units involving bonds *j*, *k*, *l*, *e*, and *m* (Figure 5c). In this case, bonds *j*, *l*, and *m* were shortened, accompanied by increased lengths of bonds *e* and *k*, during the transformation into $\text{BN-Ph}^{\bullet-}$ and BN-Ph^{2-} . These computational results suggested that, in the B \leftarrow N bridged molecule, two different yet orthogonal pathways of BLA changes were accessible to two different quinonoid constitutions during the oxidation and

in the electronic structures after the installment of the B \leftarrow N coordination. These electrochemical data demonstrated the highly efficient stabilization effect of the B \leftarrow N coordination on the oxidized/reduced states through extending charge/spin delocalization.

The excellent redox reversibility allowed spectroelectrochemical measurements on BN-Ph, i.e., UV-vis-NIR absorption spectra recorded during each of the electrochemical redox processes, which gave highly reversible multicolor electrochromism (Figure 4a). According to time-dependent DFT calculations, these drastic color changes were attributed to the substantial differences on the transition energy diagrams of the different redox states (Tables S4 and S5). When the applied potential swept from 0.70 to 1.05 V (vs Ag/AgCl), BN-Ph was gradually oxidized into the radical cation form $\text{BN-Ph}^{\bullet+}$. During this process, the HOMO-LUMO transition of the neutral BN-Ph at 768 nm diminished, while a new NIR absorption at 1180 nm emerged (Figure 4b). This low-energy absorption band corresponded to the transition of HOMO- β \rightarrow LUMO- β of the delocalized radical cation (Figure 4d), according to DFT calculation. On the basis of the cutoff shape of this NIR absorption peak, $\text{BN-Ph}^{\bullet+}$ can be categorized as a class III mixed valence system,⁵⁵ in which the two nitrogen-centered redox moieties in ICBZ were strongly coupled with one another. The absorption spectra exhibited no significant

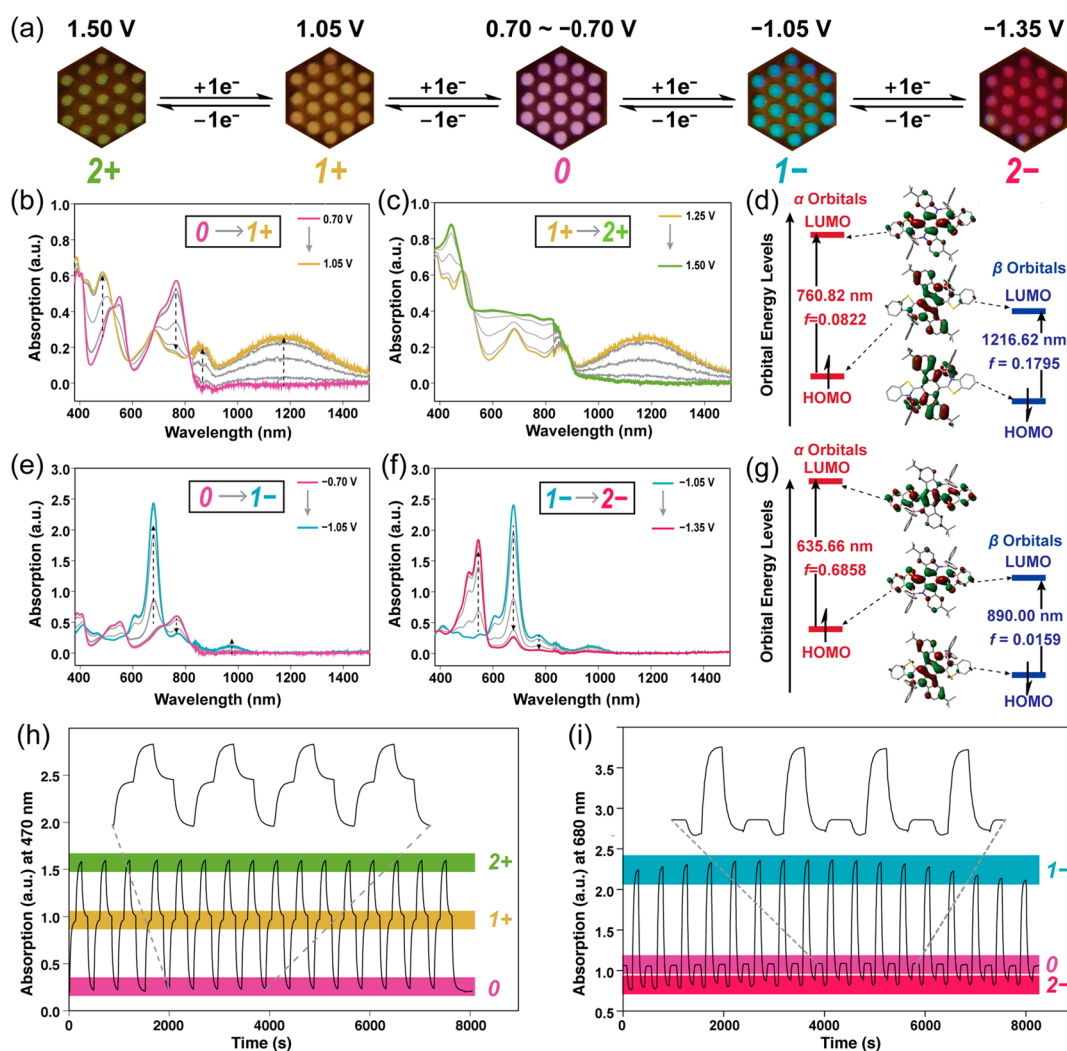


Figure 4. (a) Photographs of the **BN-Ph** solutions at different redox states in the presence of a honeycomb working electrode in a spectroelectrochemical cell (in CH_2Cl_2 with 0.10 M TBAPF₆). UV-vis-NIR absorption changes of the **BN-Ph** solutions upon stepwise applications of potentials on the honeycomb working electrode (step height = 0.05 V, vs Ag/AgCl) from (b) +0.70 to +1.05 V, (c) +1.25 to +1.50 V, (e) -0.70 to -1.05 V, and (f) -1.05 to -1.35 V. Molecular frontier orbitals and calculated transition energies of (d) **BN-Ph**^{•+} and (g) **BN-Ph**^{•-} [UB3LYP/6-311g(d,p) with CH_2Cl_2 CPCM solvation]. Multiple cycles of absorption changes of the **BN-Ph** solutions when the potential was switching between (h) 0.20, 1.10, and 1.50 V and (i) -0.30, -1.05, and -1.40 V.

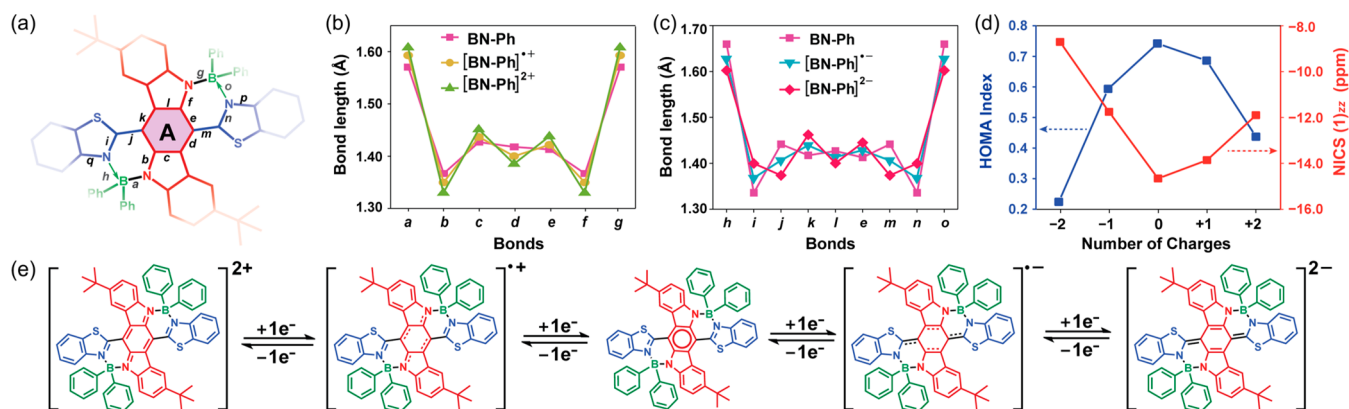


Figure 5. (a) Redox-active core structure of **BN-Ph** labeled with bond indices from *a* to *q*; (b) DFT calculated lengths of the bonds *a*–*g* before and after oxidation; (c) DFT calculated lengths of the bonds *e* and *h*–*o* before and after reduction [B3LYP/6-311g(d,p)]; (d) calculated HOMA and NICS(1)_{zz} values for the central ring “A” of **BN-Ph** in different redox states. (e) Constitutional structures of the five different redox states of **BN-Ph**.

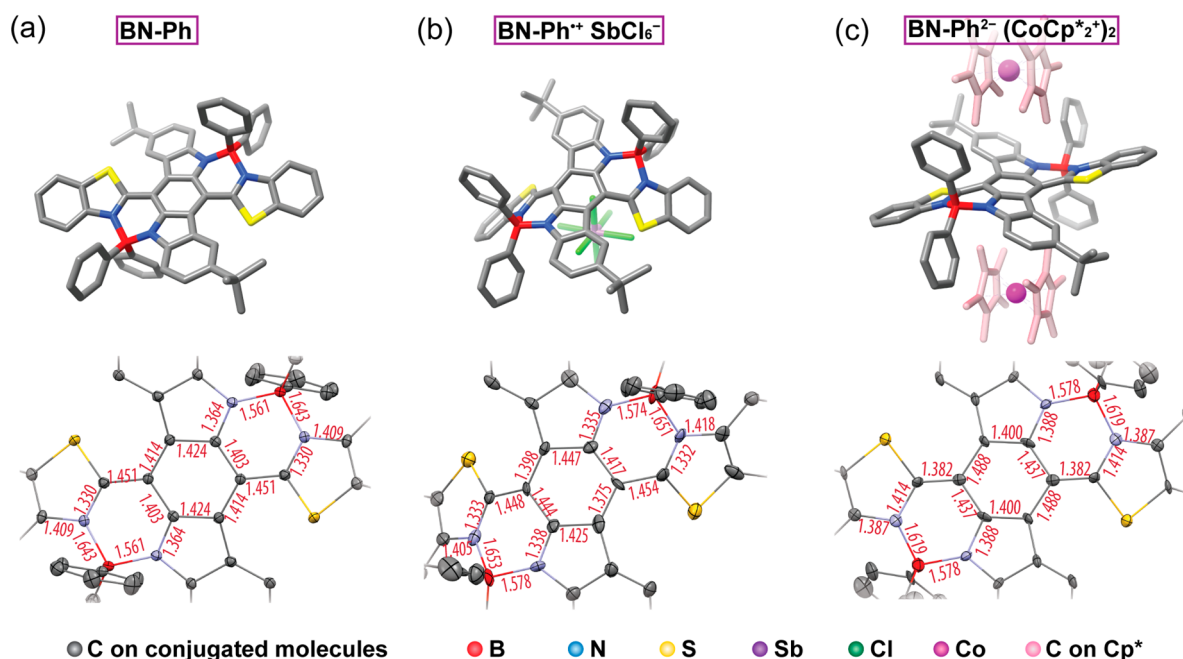


Figure 6. Single-crystal X-ray structures of (a) BN-Ph, (b) BN-Ph^{•+} SbCl₆⁻, and (c) BN-Ph²⁻ [CoCp^{*}₂]₂ and bond lengths of the area around the central ring "A". Hydrogen atoms and solvent molecules were omitted for clarity. Thermal ellipsoids are scaled to the 50% probability level.

reduction (Figure 5e), respectively, contributing to the excellent stability in all the oxidized and reduced forms of BN-Ph. Considering the noncovalent nature of B ← N coordinate bonds, the molecular geometries were also optimized at the level of B3LYP/TZVP with D3 version of Grimme's dispersion correction, which revealed similar structural transformations (Figure S15). Similar BLA changes and structural transformations were also observed in the optimized molecular geometries for different redox states of BN-F. In addition, the aromaticity of ring "A" was calculated using the harmonic oscillator model of aromaticity (HOMA) and the nucleus-independent chemical shift (NICS) values^{57–59} (Figure 5d). Both calculations confirmed a strong aromaticity of ring "A" in the neutral state and decreased aromaticity upon oxidation or reduction.

To validate these DFT computational results, the bond lengths and molecular geometries were examined by using experimental data from single-crystal X-ray diffraction of the neutral BN-Ph, the radical cation salt BN-Ph^{•+} SbCl₆⁻, and the dianion salt BN-Ph²⁻ [CoCp^{*}₂]₂ (Figure 6). The radical cation was chemically accessed by one-electron oxidation of BN-Ph with 1.2 equiv of tris(4-bromophenyl)ammoniumyl hexachloroantimonate (Magic Blue) in a CH₂Cl₂ solution. The single crystals suitable for X-ray diffraction were grown by slow vapor diffusion of pentane into a CH₂Cl₂ solution of BN-Ph^{•+} SbCl₆⁻. The dianion, on the other hand, was chemically prepared after two-electron reduction of BN-Ph by the addition of 3.0 equiv of decamethylcobaltocene (CoCp^{*}₂). Vapor diffusion of diethyl ether into a concentrated solution of BN-Ph²⁻ in acetonitrile yielded single crystals suitable for X-ray diffraction analysis. Bond lengths measured from the single-crystal structures of BN-Ph, BN-Ph^{•+} SbCl₆⁻, and BN-Ph²⁻ [CoCp^{*}₂]₂ matched well (Figure 7) with the DFT calculated bond lengths, further confirming the mechanism of the orthogonal quinonoid transformations upon oxidation and reduction, respectively. The average difference between the bond lengths calculated at the level of B3LYP/6-311g(d,p) and

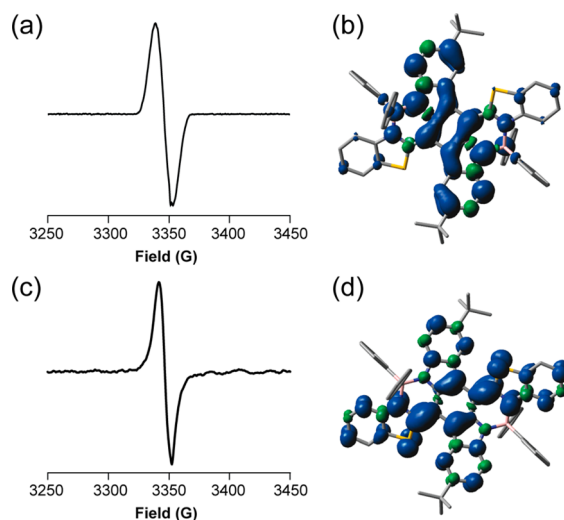


Figure 7. Electron paramagnetic resonance (EPR) spectra of (a) BN-Ph^{•+} in CH₂Cl₂ (0.13 mM) and (c) BN-Ph²⁻ in acetonitrile (0.03 mM) at 288 K. DFT computed spin density maps (isovalue = 0.0008) of (b) BN-Ph^{•+} and (d) BN-Ph²⁻ [UB3LYP/6-311g++(d,p)].

experimentally measured bond lengths was only 0.010 Å (see Table S6 for a detailed list). Such an average difference obtained from calculation at the level of B3LYP/TZVP with D3 version of Grimme's dispersion correction was also ~0.010 Å (see Table S7 for a detailed list), suggesting highly reliable computation results. The only exception was bond *d*, which was longer in the neutral state (1.444 Å) from the experimental result than that from the calculation, likely because of the steric strain between ICBZ and BTH units. In both BN-Ph^{•+} and BN-Ph²⁻, the B ← N coordinate bonds retained their strength so that the rigid backbone scaffolds were maintained. In fact, the B ← N coordinate bond was even shorter in BN-Ph²⁻ (1.619 Å) as a result of the stronger Lewis basicity of the nitrogen center on BTH after reduction. Moreover, the

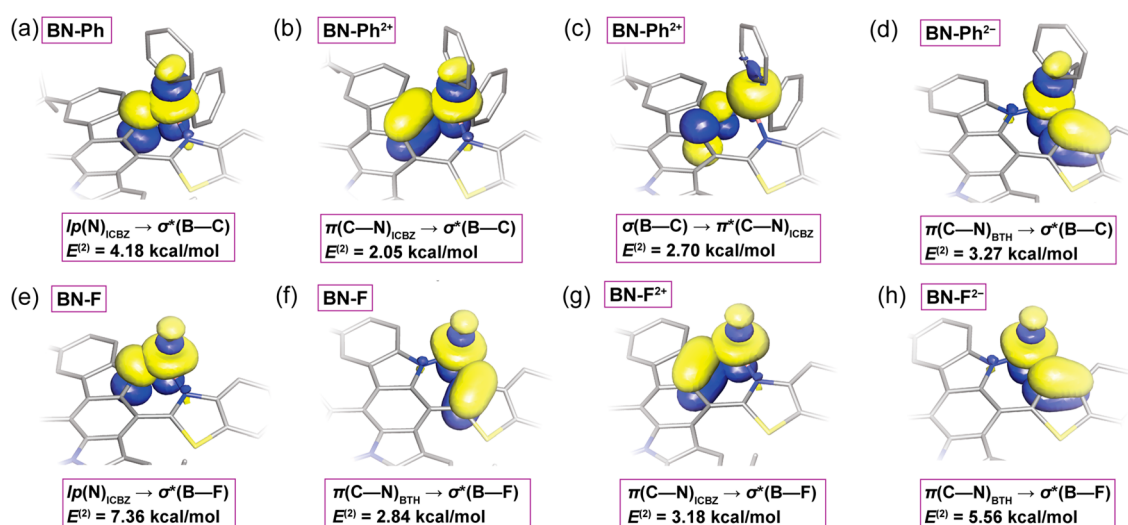


Figure 8. NBO plots of hyperconjugative interactions in different redox states of BN-Ph (a, b, c, d) and BN-F (e, f, g, h).

backbone of **BN-Ph²⁻** was more coplanar compared to that of **BN-Ph** (dihedral angles between ICBZ and BTH units reduced to 6.3°), due to an enhanced double-bond character of bonds *j* and *m*.

Additional characterizations were performed on the reduced and oxidized states of **BN-Ph** in order to further understand their electronic structures during the redox processes. Electron paramagnetic resonance (EPR) spectroscopy of the **BN-Ph⁺SbCl₆⁻** solution showed a broad resonance signal (Figure 7a). The spin concentration (7.8×10^{17} spin/mL) was close to the theoretical value (8.9×10^{17} spin/mL) when assuming the formation of an organic monoradical ($S = 1/2$) on each molecule, indicative of a high conversion from **BN-Ph** to **BN-Ph⁺**. The lack of hyperfine splitting in the EPR spectrum was attributed to the delocalized spin that experienced multiple couplings with a number of nuclei in this molecule,³⁷ in accordance with DFT computed substantial delocalization of the unpaired spin density (Figure 7b and Figure S13).

Overall, experimental investigations together with computational studies clearly revealed the underlying mechanism of the unique redox processes of ladder-type **BN-Ph** molecules, which involved two distinct pathways of constitutional changes from a benzenoid structure into two types of quinonoid structures upon oxidation and reduction, respectively. The oxidation-active moiety and reduction-active moiety were orthogonally compacted into a single molecular scaffold, giving rise to the reversible multistage redox processes. In addition, B ← N coordination promoted the rigid ladder-type structure in which separated redox centers were strongly coupled with each other, and the unpaired electron of radicals was stabilized by extensive delocalization.

In **BN-Ph** and **BN-F**, the boron centers stabilized the redox state through a number of different mechanisms, including spin coupling, extending pi-delocalization, and modulating electron densities. It was also hypothesized that the boron-ligand moieties impacted the electronic structures of these molecules through hyperconjugation similar to that existing in cyclohexa-1,3-diene (Figure 1b), providing additional stabilization effects. According to the crystal structures of **BN-Ph**, **BN-Ph⁺**, and **BN-Ph²⁻**, the two phenyl ligands on the boron center adopted different bonding orientations: one of the B–C σ -bonds was almost perpendicular to the conjugated backbone (denoted as the “axial” bond), while the other one was almost in the plane

of the backbone (denoted as the “equatorial” bond). Such an unsymmetrical geometry of the boron ligand (B–L, L = Ph or F) bonds was also predicted by DFT optimized structures of both **BN-Ph** and **BN-F**. The nonequivalent bonding orientations suggested hyperconjugative interactions between the axial bonds and the conjugated backbone in these ladder-type molecules. To unveil the hyperconjugations of these axial B–L σ/σ^* orbitals, natural bond orbital (NBO) analysis was performed on **BN-Ph**, **BN-F**, and their dianionic and dicationic forms.^{48,60} The strengths of these interactions can be correlated with second-order perturbation energies [$E^{(2)}$] computed from NBO analysis.^{61,62} In the neutral state of **BN-Ph**, a hyperconjugative donor–acceptor interaction [$E^{(2)} = 4.18 \text{ kcal/mol}$] was identified from the lone pair [$lp(N)$] on the ICBZ unit to the antibonding [$\sigma^*(B-C)$] orbital on the axial position (Figure 8a).⁶¹ After the two-electron oxidation, the quinonoid ICBZ unit of **BN-Ph²⁺** lost the lone pair on the nitrogen center and had a lower electron density. Despite a weaker electron-donating ability, the $\pi(C-N)$ orbital of the quinonoid ICBZ still interacted hyperconjugatively [$E^{(2)} = 2.05 \text{ kcal/mol}$] with the axial $\sigma^*(B-C)$ orbital (Figure 8b). More interestingly, a unique back-donating interaction [$E^{(2)} = 2.70 \text{ kcal/mol}$] was observed from the $\sigma(B-C)$ orbital to the $\pi^*(C-N)$ orbital of the electron-deficient, quinonoid ICBZ unit (Figure 8c), reinforcing the hyperconjugative stabilization effect by diluting the positive charges on the dicationic backbone of **BN-Ph²⁺**. In the reduced form of dianionic **BN-Ph²⁻**, the NBO analysis showed that the $\sigma^*(B-C)$ orbital also served as an acceptor to stabilize the negative charges on the reduced BTH units. In **BN-Ph²⁻**, bonds *p* and *q* (Figure 5a) possessed a partial double-bond character (1.387 Å in the crystal structure) so that their π orbitals participated in a hyperconjugation [$E^{(2)} = 3.27 \text{ kcal/mol}$] with the $\sigma^*(B-C)$ orbital (Figure 8d). In this case, the hyperconjugation further delocalized the negative charges and, therefore, enhanced the stability of the highly charged dianion.

In **BN-F** with the fluoride ligands, NBO analysis at different redox states demonstrated similar but even stronger hyperconjugative interactions between the axial $\sigma^*(B-F)$ orbital and the conjugated backbone, as a result of the high electronegativity of fluorine atoms (Figure 8e–h). In the optimized structure of **BN-F**, the axial $\sigma^*(B-F)$ orbitals withdrew the electron density through hyperconjugation [$E^{(2)} = 7.36 \text{ kcal/mol}$]

mol] from the electron lone pair of the nitrogen atom on the ICBZ unit (Figure 8e). Meanwhile, another donor–acceptor interaction of 2.84 kcal/mol was found in BN-F between the $\pi(\text{C}-\text{N})$ bond in the BTH unit and the axial $\sigma^*(\text{B}-\text{F})$ orbital (Figure 8f). Therefore, these profound hyperconjugative effects in BN-F, together with the inductive effect from fluorine atoms, contributed to its low-lying HOMO and LUMO levels compared to BN-Ph.

According to DFT calculation, these hyperconjugative interactions were also present in the paramagnetic radical cations and radical anions. Isotropic Fermi couplings of the axial ligands with the already delocalized spin were much higher than those of the equatorial ligands, indicating strong interactions between the axial bond with the backbone through hyperconjugation. Overall, the hyperconjugative stabilization effect further assisted the desirable charge and spin delocalization during the redox processes. Meanwhile, such orbital interactions provided an additional mechanism to impact the electronic structures and properties of the entire ladder-type molecules.

CONCLUSION

In conclusion, we demonstrated herein a molecular design strategy to achieve highly reversible, multistage redox activities and multicolor electrochromism in compact ladder-type molecules bridged with $\text{B} \leftarrow \text{N}$ coordination. The structural transformations from a benzenoid constitution into two distinct types of quinonoid constitutions during both reduction and oxidation processes were elucidated, giving a clear mechanistic picture of these robust multistage electron-transfer processes. Combined theoretical and experimental investigations demonstrated that the $\text{B} \leftarrow \text{N}$ coordination played a pivotal role in rendering the remarkable redox properties of these molecules by extending the charge and spin delocalization and by enforcing the rigid conformation. We systematically established a hyperconjugation mechanism that impacted the electronic structures and further stabilized the different redox states. These results advanced fundamental knowledge of sp^3 boron-containing π -systems, providing practical design principles for the development of p -block element-derived molecules and macromolecules with exotic optical, electronic, and spin properties, such as fully fused ladder polymers bridged by these $\text{B} \leftarrow \text{N}$ coordinate bonds.

ASSOCIATED CONTENT

Supporting Information

The Supporting Information is available free of charge on the ACS Publications website at DOI: 10.1021/jacs.8b11337.

- General methods, synthesis, characterization data, and computational data (PDF)
- Crystallographic data (CIF)
- Crystallographic data (CIF)
- Crystallographic data (CIF)
- DFT calculation optimized structures (XYZ)
- DFT calculation optimized structures (DOCX)

AUTHOR INFORMATION

Corresponding Author

*fang@chem.tamu.edu

ORCID

Congzhi Zhu: 0000-0002-1302-7187

Yi Liu: 0000-0002-3954-6102

Lei Fang: 0000-0003-4757-5664

Notes

The authors declare no competing financial interest.

ACKNOWLEDGMENTS

The authors acknowledge National Science Foundation (Award no. 1654029) and the Welch Foundation (A-1898) for financial support of this work. The authors also thank Dr. Oleg V. Ozerov and Cheng-Han Yu for the support of cyclic voltammetry measurement, Dr. Nattamai Bhuvanesh for single-crystal X-ray diffraction measurements, and the Laboratory for Molecular Simulation and High Performance Computing facilities at TAMU for providing software, support, and computer time. Work at the Molecular Foundry was supported by the Office of Science, Office of Basic Energy Sciences, of the U.S. Department of Energy under Contract no. DE-AC02-05CH11231.

REFERENCES

- (1) Lee, J.; Kalin, A. J.; Yuan, T.; Al-Hashimi, M.; Fang, L. Fully conjugated ladder polymers. *Chem. Sci.* **2017**, *8*, 2503–2521.
- (2) Zou, Y.; Ji, X.; Cai, J.; Yuan, T.; Stanton, D. J.; Lin, Y.-H.; Naraghi, M.; Fang, L. Synthesis and Solution Processing of a Hydrogen-Bonded Ladder Polymer. *Chem.* **2017**, *2*, 139–152.
- (3) Cai, Z.; Awais, M. A.; Zhang, N.; Yu, L. Exploration of Syntheses and Functions of Higher Ladder-type π -Conjugated Heteroarenes. *Chem.* **2018**, *4*, 2538–2570.
- (4) Wang, Y.; Guo, H.; Ling, S.; Arrechea-Marcos, I.; Wang, Y.; López Navarrete, J. T.; Ortiz, R. P.; Guo, X. Ladder-type Heteroarenes: Up to 15 Rings with Five Imide Groups. *Angew. Chem., Int. Ed.* **2017**, *56*, 9924–9929.
- (5) Cai, Z.; Lo, W.-Y.; Zheng, T.; Li, L.; Zhang, N.; Hu, Y.; Yu, L. Exceptional Single-Molecule Transport Properties of Ladder-Type Heteroarene Molecular Wires. *J. Am. Chem. Soc.* **2016**, *138*, 10630–10635.
- (6) Cai, Z.; Zhang, N.; Awais, M. A.; Filatov, A. S.; Yu, L. Synthesis of Alternating Donor–Acceptor Ladder-Type Molecules and Investigation of Their Multiple Charge-Transfer Pathways. *Angew. Chem., Int. Ed.* **2018**, *57*, 6442–6448.
- (7) Zheng, T.; Cai, Z.; Ho-Wu, R.; Yau, S. H.; Shaparov, V.; Goodson, T.; Yu, L. Synthesis of Ladder-Type Thienoacenes and Their Electronic and Optical Properties. *J. Am. Chem. Soc.* **2016**, *138*, 868–875.
- (8) Jin, Z.; Teo, Y. C.; Teat, S. J.; Xia, Y. Regioselective Synthesis of [3]Naphthylenes and Tuning of Their Antiaromaticity. *J. Am. Chem. Soc.* **2017**, *139*, 15933–15939.
- (9) Wang, X.-Y.; Lin, H.-R.; Lei, T.; Yang, D.-C.; Zhuang, F.-D.; Wang, J.-Y.; Yuan, S.-C.; Pei, J. Azaborine Compounds for Organic Field-Effect Transistors: Efficient Synthesis, Remarkable Stability, and BN Dipole Interactions. *Angew. Chem.* **2013**, *125*, 3199–3202.
- (10) Wang, X.-Y.; Zhuang, F.-D.; Wang, R.-B.; Wang, X.-C.; Cao, X.-Y.; Wang, J.-Y.; Pei, J. A Straightforward Strategy toward Large BN-Embedded π -Systems: Synthesis, Structure, and Optoelectronic Properties of Extended BN Heterosuperbenzenes. *J. Am. Chem. Soc.* **2014**, *136*, 3764–3767.
- (11) Stec, G. J.; Lauchner, A.; Cui, Y.; Nordlander, P.; Halas, N. J. Multicolor Electrochromic Devices Based on Molecular Plasmonics. *ACS Nano* **2017**, *11*, 3254–3261.
- (12) Wetzel, C.; Brier, E.; Vogt, A.; Mishra, A.; Mena-Osteritz, E.; Bäuerle, P. Fused Thiophene-Pyrrole-Containing Ring Systems up to a Heterodecacene. *Angew. Chem., Int. Ed.* **2015**, *54*, 12334–12338.
- (13) Gu, Y.; Wu, X.; Gopalakrishna, T. Y.; Phan, H.; Wu, J. Graphene-like Molecules with Four Zigzag Edges. *Angew. Chem., Int. Ed.* **2018**, *57*, 6541–6545.
- (14) Woodward, A. N.; Kolesar, J. M.; Hall, S. R.; Saleh, N.-A.; Jones, D. S.; Walter, M. G. Thiazolothiazole Fluorophores Exhibiting

- 600 Strong Fluorescence and Viologen-Like Reversible Electrochromism.
601 *J. Am. Chem. Soc.* **2017**, *139*, 8467–8473.
- 602 (15) Li, G.; Xu, L.; Zhang, W.; Zhou, K.; Ding, Y.; Liu, F.; He, X.;
603 He, G. Narrow-Bandgap Chalcogenoviologens for Electrochromism
604 and Visible-Light-Driven Hydrogen Evolution. *Angew. Chem., Int. Ed.*
605 **2018**, *57*, 4897–4901.
- 606 (16) Wakamiya, A.; Taniguchi, T.; Yamaguchi, S. Intramolecular B–
607 N Coordination as a Scaffold for Electron-Transporting Materials:
608 Synthesis and Properties of Boryl-Substituted Thienylthiazoles.
609 *Angew. Chem., Int. Ed.* **2006**, *45*, 3170–3173.
- 610 (17) Crossley, D. L.; Cade, I. A.; Clark, E. R.; Escande, A.;
611 Humphries, M. J.; King, S. M.; Vitorica-Yrezabal, I.; Ingleson, M. J.;
612 Turner, M. L. Enhancing electron affinity and tuning band gap in
613 donor–acceptor organic semiconductors by benzothiadiazole directed
614 C–H borylation. *Chem. Sci.* **2015**, *6*, 5144–5151.
- 615 (18) Grandl, M.; Sun, Y.; Pammer, F. Generation of an N→B
616 Ladder-type Structure by Regioselective Hydroboration of an Alkenyl-
617 Functionalized Quaterpyridine. *Chem. - Eur. J.* **2016**, *22*, 3976–3980.
- 618 (19) Zhu, C.; Guo, Z.-H.; Mu, A. U.; Liu, Y.; Wheeler, S. E.; Fang, L.
619 Low Band Gap Coplanar Conjugated Molecules Featuring Dynamic
620 Intramolecular Lewis Acid–Base Coordination. *J. Org. Chem.* **2016**,
621 *81*, 4347–4352.
- 622 (20) Zhu, C.; Fang, L. Locking the Coplanar Conformation of π -
623 Conjugated Molecules and Macromolecules Using Dynamic Non-
624 covalent Bonds. *Macromol. Rapid Commun.* **2018**, *39*, 1700241.
- 625 (21) Huang, H.; Yang, L.; Facchetti, A.; Marks, T. J. Organic and
626 Polymeric Semiconductors Enhanced by Noncovalent Conforma-
627 tional Locks. *Chem. Rev.* **2017**, *117*, 10291–10318.
- 628 (22) Shimogawa, H.; Yoshikawa, O.; Aramaki, Y.; Murata, M.;
629 Wakamiya, A.; Murata, Y. 4,7-Bis[3-(dimesitylboryl)thien-2-yl]-
630 benzothiadiazole: Solvato-, Thermo-, and Mechanochromism Based
631 on the Reversible Formation of an Intramolecular B–N Bond. *Chem. -*
632 *Eur. J.* **2017**, *23*, 3784–3791.
- 633 (23) Dou, C.; Long, X.; Ding, Z.; Xie, Z.; Liu, J.; Wang, L. An
634 Electron-Deficient Building Block Based on the B ← N Unit: An
635 Electron Acceptor for All-Polymer Solar Cells. *Angew. Chem., Int. Ed.*
636 **2016**, *55*, 1436–1440.
- 637 (24) Rao, Y.-L.; Amarne, H.; Zhao, S.-B.; McCormick, T. M.;
638 Martić, S.; Sun, Y.; Wang, R.-Y.; Wang, S. Reversible Intramolecular
639 C–C Bond Formation/Breaking and Color Switching Mediated by a
640 N,C-Chelate in (2-ph-py)BMes2 and (5-BMes2–2-ph-py)BMes2. *J.*
641 *Am. Chem. Soc.* **2008**, *130*, 12898–12900.
- 642 (25) Liu, K.; Lalancette, R. A.; Jäkle, F. B–N Lewis Pair
643 Functionalization of Anthracene: Structural Dynamics, Optoelec-
644 tronic Properties, and O2 Sensitization. *J. Am. Chem. Soc.* **2017**, *139*,
645 18170–18173.
- 646 (26) Yusuf, M.; Liu, K.; Guo, F.; Lalancette, R. A.; Jäkle, F.
647 Luminescent organoboron ladder compounds via directed electro-
648 philic aromatic C–H borylation. *Dalton Trans.* **2016**, *45*, 4580–4587.
- 649 (27) Wakamiya, A.; Murakami, T.; Yamaguchi, S. Benzene-fused
650 BODIPY and fully-fused BODIPY dimer: impacts of the ring-fusing at
651 the b bond in the BODIPY skeleton. *Chem. Sci.* **2013**, *4*, 1002–1007.
- 652 (28) Alahmadi, A. F.; Lalancette, R. A.; Jäkle, F. Highly Luminescent
653 Ladderized Fluorene Copolymers Based on B–N Lewis Pair
654 Functionalization. *Macromol. Rapid Commun.* **2018**, *39*, 1800456.
- 655 (29) Dou, C.; Liu, J.; Wang, L. Conjugated polymers containing B←
656 N unit as electron acceptors for all-polymer solar cells. *Sci. China:*
657 *Chem.* **2017**, *60*, 450–459.
- 658 (30) Qiu, F.; Zhang, F.; Tang, R.; Fu, Y.; Wang, X.; Han, S.; Zhuang,
659 X.; Feng, X. Triple Boron-Cored Chromophores Bearing Discotic
660 5,11,17-Triazatrinaphthylene-Based Ligands. *Org. Lett.* **2016**, *18*,
661 1398–1401.
- 662 (31) Wang, X.-Y.; Narita, A.; Feng, X.; Müllen, K. B2N2-
663 Dibenzo[a,e]pentalenes: Effect of the BN Orientation Pattern on
664 Antiaromaticity and Optoelectronic Properties. *J. Am. Chem. Soc.*
665 **2015**, *137*, 7668–7671.
- 666 (32) Wang, X.-Y.; Wang, J.-Y.; Pei, J. BN Heterosuperbenzenes:
667 Synthesis and Properties. *Chem. - Eur. J.* **2015**, *21*, 3528–3539.
- (33) Hou, Q.; Liu, L.; Møllerup, S. K.; Wang, N.; Peng, T.; Chen, P.; 668
Wang, S. Stimuli-Responsive B/N Lewis Pairs Based on the 669
Modulation of B–N Bond Strength. *Org. Lett.* **2018**, *20*, 6467–6470. 670
- (34) Yang, D.-T.; Møllerup, S. K.; Peng, J.-B.; Wang, X.; Li, Q.-S.; 671
Wang, S. Substituent Directed Phototransformations of BN-Hetero- 672
cycles: Elimination vs Isomerization via Selective B–C Bond 673
Cleavage. *J. Am. Chem. Soc.* **2016**, *138*, 11513–11516. 674
- (35) Grandl, M.; Rudolf, B.; Sun, Y.; Bechtel, D. F.; Pierik, A. J.; 675
Pammer, F. Intramolecular N → B Coordination as a Stabilizing 676
Scaffold for π -Conjugated Radical Anions with Tunable Redox 677
Potentials. *Organometallics* **2017**, *36*, 2527–2535. 678
- (36) Su, Y.; Kinjo, R. Boron-containing radical species. *Coord. Chem.* 679
Rev. **2017**, *352*, 346–378. 680
- (37) Ji, L.; Edkins, R. M.; Lorbach, A.; Krummenacher, I.; Brückner, 681
C.; Eichhorn, A.; Braunschweig, H.; Engels, B.; Low, P. J.; Marder, T. 682
B. Electron Delocalization in Reduced Forms of 2-(BMes2)pyrene 683
and 2,7-Bis(BMes2)pyrene. *J. Am. Chem. Soc.* **2015**, *137*, 6750–6753. 684
- (38) Ji, L.; Griesbeck, S.; Marder, T. B. Recent developments in and 685
perspectives on three-coordinate boron materials: a bright future. 686
Chem. Sci. **2017**, *8*, 846–863. 687
- (39) Luo, D.; Lee, S.; Zheng, B.; Sun, Z.; Zeng, W.; Huang, K.-W.; 688
Furukawa, K.; Kim, D.; Webster, R. D.; Wu, J. Indolo[2,3- 689
b]carbazoles with tunable ground states: how Clar’s aromatic sextet 690
determines the singlet biradical character. *Chem. Sci.* **2014**, *5*, 4944– 691
4952. 692
- (40) Janosik, T.; Rannug, A.; Rannug, U.; Wahlström, N.; Slätt, J.; 693
Bergman, J. Chemistry and Properties of Indolocarbazoles. *Chem. Rev.* 694
2018, *118*, 9058–9128. 695
- (41) Maeda, C.; Todaka, T.; Ueda, T.; Ema, T. Synthesis of 696
carbazole-based BODIPY dimers showing red fluorescence in the 697
solid state. *Org. Biomol. Chem.* **2017**, *15*, 9283–9287. 698
- (42) Maeda, C.; Nagahata, K.; Ema, T. Carbazole-based BODIPYs 699
with ethynyl substituents at the boron center: solid-state excimer 700
fluorescence in the VIS/NIR region. *Org. Biomol. Chem.* **2017**, *15*, 701
7783–7788. 702
- (43) Curiel, D.; Más-Montoya, M.; Usea, L.; Espinosa, A.; Orenes, 703
R. A.; Molina, P. Indolocarbazole-Based Ligands for Ladder-Type 704
Four-Coordinate Boron Complexes. *Org. Lett.* **2012**, *14*, 3360–3363. 705
- (44) Knowles, C. M.; Watt, G. W. The Reduction of Benzoxazoles 706
and Benzothiazoles in Liquid Ammonia. *J. Org. Chem.* **1942**, *07*, 56– 707
62. 708
- (45) Ulrich, G.; Ziesse, R.; Harriman, A. The Chemistry of 709
Fluorescent Bodipy Dyes: Versatility Unsurpassed. *Angew. Chem., Int.* 710
Ed. **2008**, *47*, 1184–1201. 711
- (46) Loudet, A.; Burgess, K. BODIPY Dyes and Their Derivatives: 712
Syntheses and Spectroscopic Properties. *Chem. Rev.* **2007**, *107*, 4891– 713
4932. 714
- (47) Mehta, G.; Uma, R. Stereoelectronic Control in Diels–Alder 715
Reaction of Dissymmetric 1,3-Dienes. *Acc. Chem. Res.* **2000**, *33*, 278– 716
286. 717
- (48) Alabugin, I. V.; Gilmore, K. M.; Peterson, P. W. Hyper- 718
conjugation. *Wiley Interdiscip. Rev. Comput. Mol. Sci.* **2011**, *1*, 109– 719
141. 720
- (49) Ajayakumar, M. R.; Asthana, D.; Mukhopadhyay, P. Core- 721
Modified Naphthalenediimides Generate Persistent Radical Anion 722
and Cation: New Panchromatic NIR Probes. *Org. Lett.* **2012**, *14*, 723
4822–4825. 724
- (50) Yao, C.-J.; Zhong, Y.-W.; Nie, H.-J.; Abruña, H. D.; Yao, J. 725
Near-IR Electrochromism in Electropolymerized Films of a 726
Biscyclometalated Ruthenium Complex Bridged by 1,2,4,5-Tetra(2- 727
pyridyl)benzene. *J. Am. Chem. Soc.* **2011**, *133*, 20720–20723. 728
- (51) Dyer, A. L.; Grenier, C. R. G.; Reynolds, J. R. A Poly(3,4- 729
alkylenedioxythiophene) Electrochromic Variable Optical Attenuator 730
with Near-Infrared Reflectivity Tuned Independently of the Visible 731
Region. *Adv. Funct. Mater.* **2007**, *17*, 1480–1486. 732
- (52) Mortimer, R. J. Electrochromic Materials. *Annu. Rev. Mater. Res.* 733
2011, *41*, 241–268. 734

- (53) Mee, S. P. H.; Lee, V.; Baldwin, J. E. Stille Coupling Made Easier—The Synergic Effect of Copper(I) Salts and the Fluoride Ion. *Angew. Chem., Int. Ed.* **2004**, *43*, 1132–1136.
- (54) Jiang, W.; Tang, J.; Ban, X.; Sun, Y.; Duan, L.; Qiu, Y. Ideal Bipolar Host Materials with Bis-benzimidazole Unit for Highly Efficient Solution-Processed Green Electrophosphorescent Devices. *Org. Lett.* **2014**, *16*, 5346–5349.
- (55) Hankache, J.; Wenger, O. S. Organic Mixed Valence. *Chem. Rev.* **2011**, *111*, 5138–5178.
- (56) Hansmann, M. M.; Melaimi, M.; Bertrand, G. Organic Mixed Valence Compounds Derived from Cyclic (Alkyl)(amino)carbenes. *J. Am. Chem. Soc.* **2018**, *140*, 2206–2213.
- (57) Krygowski, T. M.; Cyrański, M. K. Structural Aspects of Aromaticity. *Chem. Rev.* **2001**, *101*, 1385–1420.
- (58) Ke, X.-S.; Hong, Y.; Lynch, V. M.; Kim, D.; Sessler, J. L. Metal-Stabilized Quinoidal Dibenzo[*g,p*]chrysene-Fused Bis-dicarbacorrole System. *J. Am. Chem. Soc.* **2018**, *140*, 7579–7586.
- (59) Lu, T.; Chen, F. Multiwfn: A multifunctional wavefunction analyzer. *J. Comput. Chem.* **2012**, *33*, 580–592.
- (60) Tomoda, S.; Senju, T. Natural bond orbital analysis of hyperconjugative stabilization effects in the transition states of cyclohexanone reduction with LiAlH₄. *Chem. Commun.* **1999**, 423–424.
- (61) Kwon, O.; Sevin, F.; McKee, M. L. Density Functional Calculations of Methylolithium, *t*-Butyllithium, and Phenyllithium Oligomers: Effect of Hyperconjugation on Conformation. *J. Phys. Chem. A* **2001**, *105*, 913–922.
- (62) Alam Sk, M.; Xi, H.-W.; Lim, K. H. Structure, Bonding, and Hyperconjugation of Germaallene: A Theoretical Study. *Organo-metallics* **2009**, *28*, 3678–3685.